LETTER

doi:10.1038/nature23657

Molecular machines open cell membranes

Víctor García-López[1,2], Fang Chen[3], Lizanne G. Nilewski[1,2], Guillaume Duret[4], Amir Aliyan[1], Anatoly B. Kolomeisky[1], Jacob T. Robinson[4], Gufeng Wang[3], Robert Pal[5] & James M. Tour[1,2,6]

Beyond the more common chemical delivery strategies, several physical techniques are used to open the lipid bilayers of cellular membranes[1]. These include using electric[2] and magnetic[3] fields, temperature[4], ultrasound[5] or light[6] to introduce compounds into cells, to release molecular species from cells or to selectively induce programmed cell death (apoptosis) or uncontrolled cell death (necrosis). More recently, molecular motors and switches that can change their conformation in a controlled manner in response to external stimuli have been used to produce mechanical actions on tissue for biomedical applications[7–9]. Here we show that molecular machines can drill through cellular bilayers using their molecular-scale actuation, specifically nanomechanical action. Upon physical adsorption of the molecular motors onto lipid bilayers and subsequent activation of the motors using ultraviolet light, holes are drilled in the cell membranes. We designed molecular motors and complementary experimental protocols that use nanomechanical action to induce the diffusion of chemical species out of synthetic vesicles, to enhance the diffusion of traceable molecular machines into and within live cells, to induce necrosis and to introduce chemical species into live cells. We also show that, by using molecular machines that bear short peptide addends, nanomechanical action can selectively target specific cell-surface recognition sites. Beyond the *in vitro* applications demonstrated here, we expect that molecular machines could also be used *in vivo*, especially as their design progresses to allow two-photon, near-infrared and radio-frequency activation[10].

A scheme for nanomechanical action on a lipid bilayer is shown in Fig. 1a and the general design of a molecular machine that is suitable for transport through a lipid bilayer is shown in Fig. 1b. These molecular machines include molecular motors that bear fluorophores for tracking (**1** and **2**), smaller nanomachines (**3** and **4**), a control that bears a stator but no rotor (**5**), a control analogue (**6**) that can undergo only *cis–trans* isomerization (flapping) at room temperature, and targeting systems that bear peptide sequences for binding to specific cell-surface receptors (**7**–**10**) (Fig. 1c)[11–14]. Molecular machine **1** has previously been shown to display enhanced diffusion in solution when the fast light-driven motor is activated by 355–365-nm ultraviolet (UV) light[15]. We conjecture that similar motor-bearing nanomachines could be activated while physisorbed on lipid membranes.

First, synthetic bilipid vesicles were opened using nanomachine **1** to release boron dipyrromethene (BODIPY) dyes that were co-encapsulated with **1** in the vesicle (Supplementary Fig. 2). We studied the release of BODIPY dye molecules encapsulated in a bilipid vesicle (but not bound to the nanomachine) by using UV exposure and observed little release of the BODIPY dye from the synthetic vesicle. Next, BODIPY and **1** were co-encapsulated in the bilipid vesicles and a UV-light-emitting diode was used as the activation source for **1** (Supplementary Fig. 3). As the UV irradiation time increased, the fluorescence intensity of the vesicles decreased as BODIPY and **1** diffused out of the vesicles, suggesting nanomechanical disruption of the vesicle bilipid membranes. We used a series of control molecules to exclude the possibility that the large decrease in fluorescence intensity in the vesicles that contained the mixture of BODIPY and **1** was caused by UV-light-induced photo-bleaching. We found that the thermal effects due to the absorption of UV light by **1** was not responsible for the vesicle opening: a control molecule that has an even larger absorption coefficient at 365 nm than that of **1** did not exhibit loss of BODIPY fluorescence from the vesicles (Supplementary Fig. 3).

After the synthetic bilipid vesicle experiments, we studied nanomechanical action on live cells by using confocal microscopy aided by a super-resolution technique called phase modulation nanoscopy (see Supplementary Information)[16,17]. We used two experimental methods, whereby either: (A) the molecular motors were loaded into the cell media and the imaging was initiated within 5 min to 24 h; or (B) the molecular motors were loaded into the cell media, incubated for 30 min to 24 h and then washed three times with fresh molecular-motor-free media before imaging.

We first studied the effect of the nanomachines on the cells without exposure to UV light (Fig. 2a, b). Using method A, molecular machines **1** (excitation wavelength $\lambda_{ex} = 633$ nm, emission wavelength $\lambda_{em} = 650–680$ nm for the pendant cy5 dyes) and **2** ($\lambda_{ex} = 514$ nm, $\lambda_{em} = 530–580$ nm for the pendant BODIPY dyes) do not induce accelerated necrosis when introduced into mouse embryonic fibroblast (NIH 3T3) cells. However, because **1** and **2** have pronounced visible fluorescence properties corresponding to the cy5 and BODIPY addends (Supplementary Fig. 4, Supplementary Table 1), respectively, their intracellular uptake, motion, or protein- or organelle-assisted trafficking are clearly observed. The two luminescent compounds display very different localization patterns. Nanomachine **2** enters the cell and localizes in the mitochondria (Fig. 2a). Conversely, when introduced to cells, **1** displays pit-like cell-surface localization (Fig. 2b, Supplementary Videos 1 and 2), and after 4 h small (approximately 1 μm) aggregates are seen inside the cytoplasm. We observed these time-dependent localization patterns to be constant within the applied 0.10–1.00 μM final nanomachine loading concentrations, suggestive of an active uptake mechanism. We undertook a series of control experiments to confirm the active uptake of the molecular motors by endocytosis. This was done using a range of nanomachine loading concentrations (0.10–1.00 μM, method A) and an incubation time of 5–60 min (with 4-h pre-incubation for temperature equilibration) at 4 °C, a temperature at which endocytosis is generally inhibited[18,19]. These studies reveal no detectable localized fluorescence of **2** in the mitochondria or of **1** on the cell surface. Our experiments eliminate the possibility of passive concentration-gradient-driven diffusion or static cell-surface interactions of these nanomachines. Further strengthening this observation are the fluorescence intensity measurements that demonstrate that more than 99% of the motors applied could be recycled from the wash solutions and re-collected during loading and imaging. Because we did not UV-activate the motors in the experiment for Fig 2a, b, we did not see accelerated cell death. Cell viability throughout these experiments remained at more than 90%, and both fluorescent nanomachines **1** and **2** were found to be non-toxic in the applied time and concentration regimes.

[1]Department of Chemistry, Rice University, Houston, Texas 77005, USA. [2]Smalley-Curl Institute and NanoCarbon Center, Rice University, Houston, Texas 77005, USA. [3]Department of Chemistry, North Carolina State University, Raleigh, North Carolina 27695, USA. [4]Department of Electrical and Computer Engineering, Rice University, Houston, Texas 77005, USA. [5]Department of Chemistry, Durham University, South Road, Durham DH1 3LE, UK. [6]Department of Materials Science and NanoEngineering, Rice University, Houston, Texas 77005, USA.

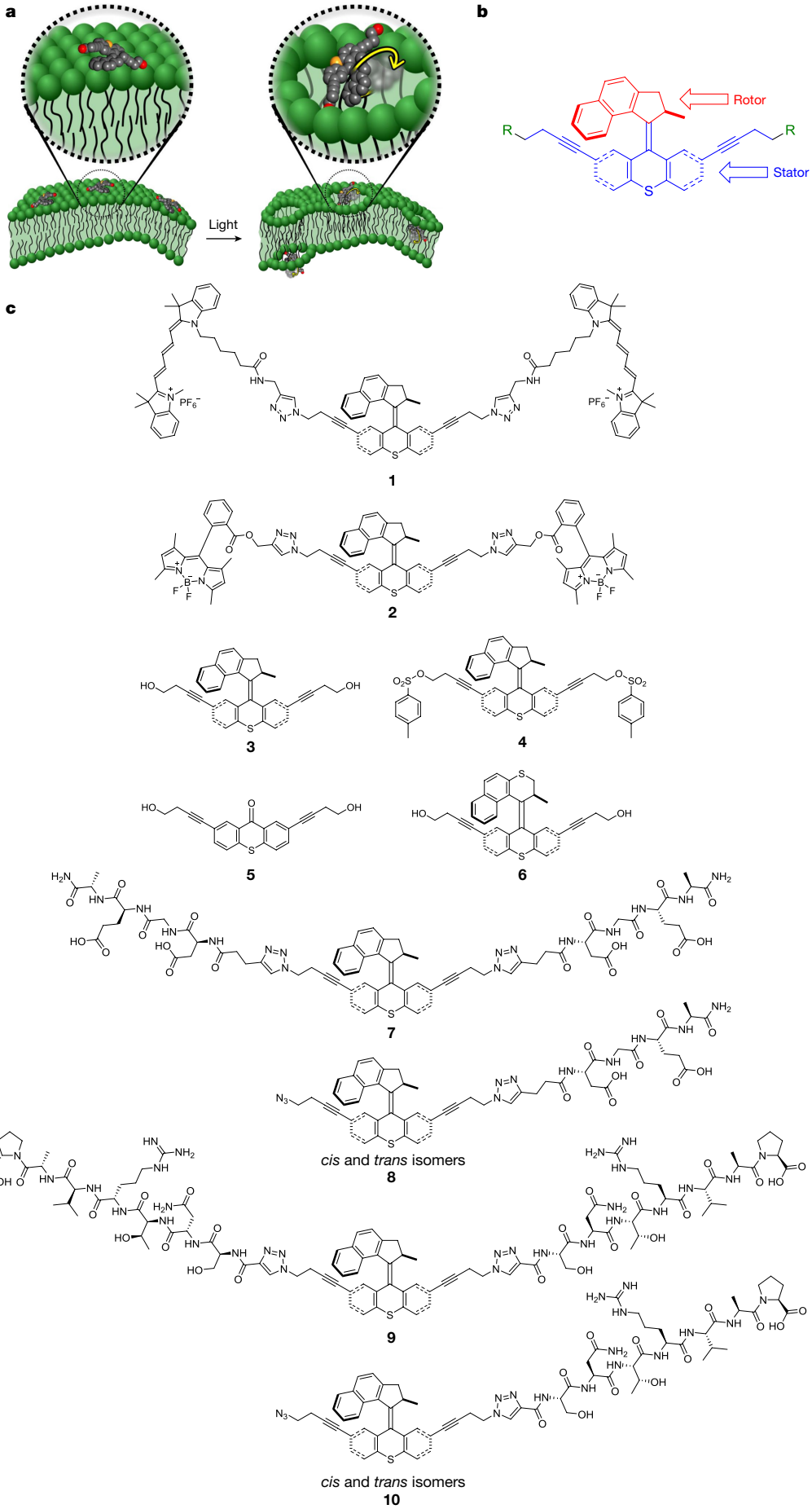

Figure 1 | Molecular motors for disruption of lipid bilayers through molecular mechanical action and control molecules. **a**, Schematic of molecular machines atop a cell membrane (left). The membrane is then opened by UV-activated nanomechanical action (indicated by a yellow arrow; right). **b**, The representative molecular machine shows the rotor portions (red), which are light-activated to rotate relative to the larger stator portion (blue); the functional addends (R; green) can be varied to provide the requisite solubility, fluorophores for tracking or recognition sites for cellular targeting. **c**, Nanomachines **1** and **2** bear fluorophores as pendants on the stator portions for tracking their movement, whereas **3** and **4** have smaller molecular sizes with no stator-addended fluorophores for their tracking. Compound **5** has a stator segment but no rotor; this serves as a control molecule that cannot be UV activated. Likewise, **6** has a slow rotor which serves as a control. Nanomachines **7** and **8** are functionalized with the peptide sequence DGEA to target $\alpha_2\beta_1$-integrin, which is overexpressed in PC-3 human prostate cancer cells. **9** and **10** are functionalized with the peptide SNTRVAP to bind to the 78-kDa glucose-regulated protein (GRP78), which targets castrate-resistant osteogenic prostate cancer receptors on PC-3 human prostate cancer cells. Rotors in nanomachines **1**–**4** and **7**–**10** rotate at 2–3 MHz when activated with 355–365-nm light; **6** rotates at 1.8 revolutions per hour when activated with 355–365-nm light at a temperature of 60 °C, but undergoes only *cis*–*trans* isomerization about the rotor–stator double bond at room temperature. The syntheses are described in Supplementary Methods and Supplementary Scheme 1, along with the photo-induced interconversion of the *cis* and *trans* isomers of **8** (Supplementary Fig. 1).

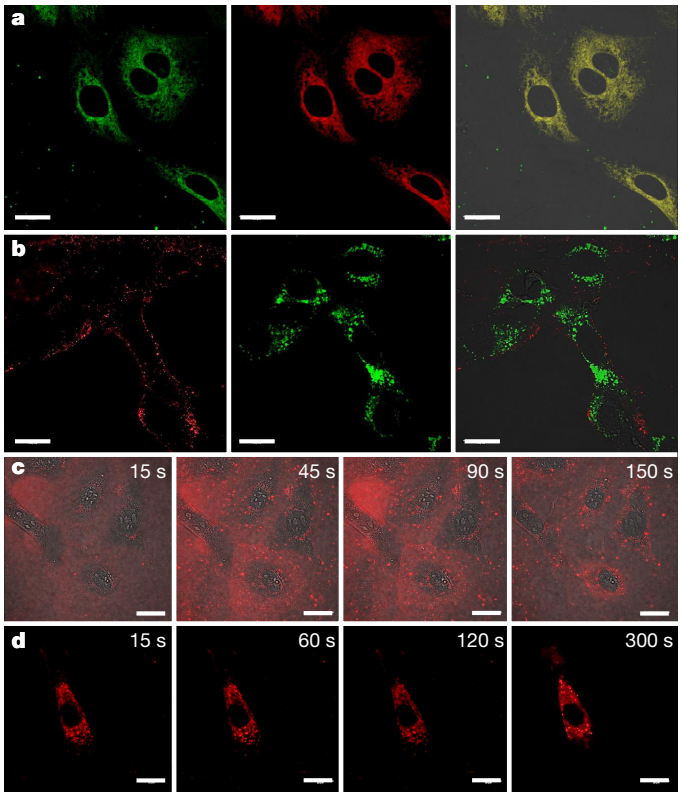

Figure 2 | NIH 3T3 cells in the presence of the fluorescent molecular machines 1 and 2. UV activation was used to cause nanomechanical-induced entry of **1** and **2** into the cells. **a**, Nanomachine **2** without UV activation of the motor. Left: green, loading concentration $C_{loading} = 500$ nM for 2 h, $\lambda_{ex} = 514$ nm, $\lambda_{em} = 520–540$ nm, 2 mW. Middle: MitoTrackerRed, $C_{loading} = 100$ nM for 30 min, $\lambda_{ex} = 543$ nm, $\lambda_{em} = 550–600$ nm, 0.5 mW. The right panel shows the two (left and middle) merged transmission images, verifying mitochondrial localization. **b**, Nanomachine **1** without UV activation of the motor. Left: red, $C_{loading} = 500$ nM for 1 h, $\lambda_{ex} = 633$ nm, $\lambda_{em} = 650–700$ nm, 1 mW. Middle: LysoTrackerGreen, $C_{loading} = 200$ nM for 5 min, $\lambda_{ex} = 488$ nm, $\lambda_{em} = 500–530$ nm, 0.2 mW. The right panel shows the two merged transmission images, highlighting pit-like surface localization. **c**, Merged transmission (488 nm, 0.2 mW) images demonstrating time-dependent internalization of **1** upon UV activation of the motor that was achieved using parallel $\lambda_{ex} = 355$ nm, 20 mW and 400 nJ per voxel. The total dwell time is noted in each image. See Supplementary Videos 4 and 5. **d**, Fluorescent images demonstrating time-dependent dispersion of intracellular aggregates of **1**, which formed after 1 h of incubation and wash cycles followed by UV activation of the motor for the times noted in each image. All scale bars, 20 μm.

The NIH 3T3 cells in the presence of the nanomachines were then studied with concomitant UV activation of the motors (Fig 2c, d). Upon UV-induced motor activation for 150 s (355 nm), **1**, introduced by method A, was found to cross the cell membrane and was internalized into cells in a time-dependent manner, displaying accelerated intracellular motion (Supplementary Videos 3–5) compared to the natural movement of homeostatic cellular organelles in the absence of nanomechanical UV activation (Fig. 2c, Supplementary Video 6). Combined, controlled time- and UV-exposure-dependent experiments indicate that the small aggregates of **1** inside the cytoplasm dissolve or burst with further increases in the fluorescence signal in the cytoplasm (Fig. 2d; compare Supplementary Videos 3–5 with Supplementary Videos 7 and 8). Nanomachine trafficking can thus be facilitated and precisely observed.

We then used the smaller nanomachine, **3**. Initial control experiments (blank) were performed without nanomachines being present. UV-induced (355 nm) human prostate adenocarcinoma cell (PC-3) necrosis was not initiated until approximately scan 20 (corresponding to 300 s of continuous scanning UV exposure, 400 nJ per voxel of total dwell time) and was characterized by massive disruption and rupture of the mitochondrial network and a subsequent, pronounced auto-fluorescent signal that was detectable in the nucleoli and nucleus wall (Fig. 3a). This signal is observable by the nucleoli membrane permeabilization and DNA damage at the onset of necrosis. The UV-induced necrosis reaches the final stages at approximately scan 40 (corresponding to 600 s), consistent with characteristic extracellular membrane rupture and homogenous cytosolic auto-fluorescence, indicating loss of cellular organelle boundaries. Conversely, visual signs of apoptosis include cell shrivelling and subsequent detachment from the coverslip surface, followed by fragmentation. Using **3** (introduced by method A) with both PC-3 and NIH 3T3 cell lines in the time- and UV-exposure-dependent *in vitro* microscopy experiments with the previously established standard experimental parameters and 355-nm laser exposure, we observed that cell death was accelerated by more than 50% relative to UV exposure without **3**, owing to disruption of the cell membrane (Fig. 3b, Supplementary Fig. 5). Pronounced fragmentation of the mitochondrial network is established between scans 8 and 10 (corresponding to 120 s and 150 s, respectively), with bursting of the extracellular membrane manifesting at scan 20 (300 s) (Supplementary Table 2, Supplementary Fig. 5); this is confirmation of accelerated necrosis. Importantly, **3** was found to be non-internalizing before UV activation; the onset of necrosis and the fragmentation of organelle mitochondria or damage to the nucleolus within the cell were identical regardless of whether the cells were incubated with **3** for 2–4 h before UV activation or **3** was added directly before UV activation.

We studied molecular machine **4** by using identical pre-set study parameters and method A on both PC-3 and NIH 3T3 cells. UV-induced nanomechanical action caused necrosis only 10% earlier (Supplementary Table 2) than when using the standard blank reference cells that do not contain molecular motors (Fig. 3c, Supplementary Fig. 5). Nanomachine **4**, which bears the larger aryl sulfonate moieties, might have been inhibited from having its rotor physisorb well within the cell membranes, or the larger addends themselves might have sterically encumbered transport through the membrane.

We studied the rotor-free control molecule **5**, which has the same homopropargylic alcohol stator moieties as does **3**, to ensure that the rotary action is essential for the bilayer perturbations. Using method A on both PC-3 and NIH 3T3 cells, control molecule **5** shows no effect on necrosis upon standardized UV exposure (Fig. 3d, Supplementary Fig. 5). This finding further suggests that the accelerated cell death seen when using **3** was not primarily due to the short exposure to UV light or subsequent thermal processes, similarly to our synthetic bilayer studies.

To further ensure that fast rotary motion is essential for nanomechanical opening of cells, another control (**6**) was used, which bears a six-membered heterocyclic rotor that is nearly identical in molecular size and functionality to **3**. However, **6** can undergo only *cis–trans* isomerization upon light activation at room temperature. This 'flapping' action will occur without full rotation because that barrier (rotor crossing over the stator) requires a temperature of 60 °C in the heterocyclic system[15]. Even at 60 °C, the rotation rate is only about two revolutions per hour, as opposed to the nearly identical molecular-sized **3**, which rotates at 2–3 MHz upon UV activation at room temperature. Compound **6** showed no enhanced necrosis in PC-3 or NIH 3T3 cells upon standardized UV exposure (Supplementary Fig. 6). Furthermore, a compound analogous to **3** but without the allylic methyl, which therefore can rotate but not unidirectionally, was only slightly faster than the motor-free system (Supplementary Fig. 6). Therefore, as suggested by Purcell[20], the non-reciprocating unidirectional motor rotation is the highly preferred mode for these nanomachines, which have ultralow Reynolds numbers, while progressing through the lipid bilayers.

We further confirmed the nanomechanical opening and subsequent permeabilization of the membrane by adding an exogenous dye to the cell medium to assess its entry into the cells that might be afforded by nanomechanical action. Using PC-3 cells and **3**, propidium

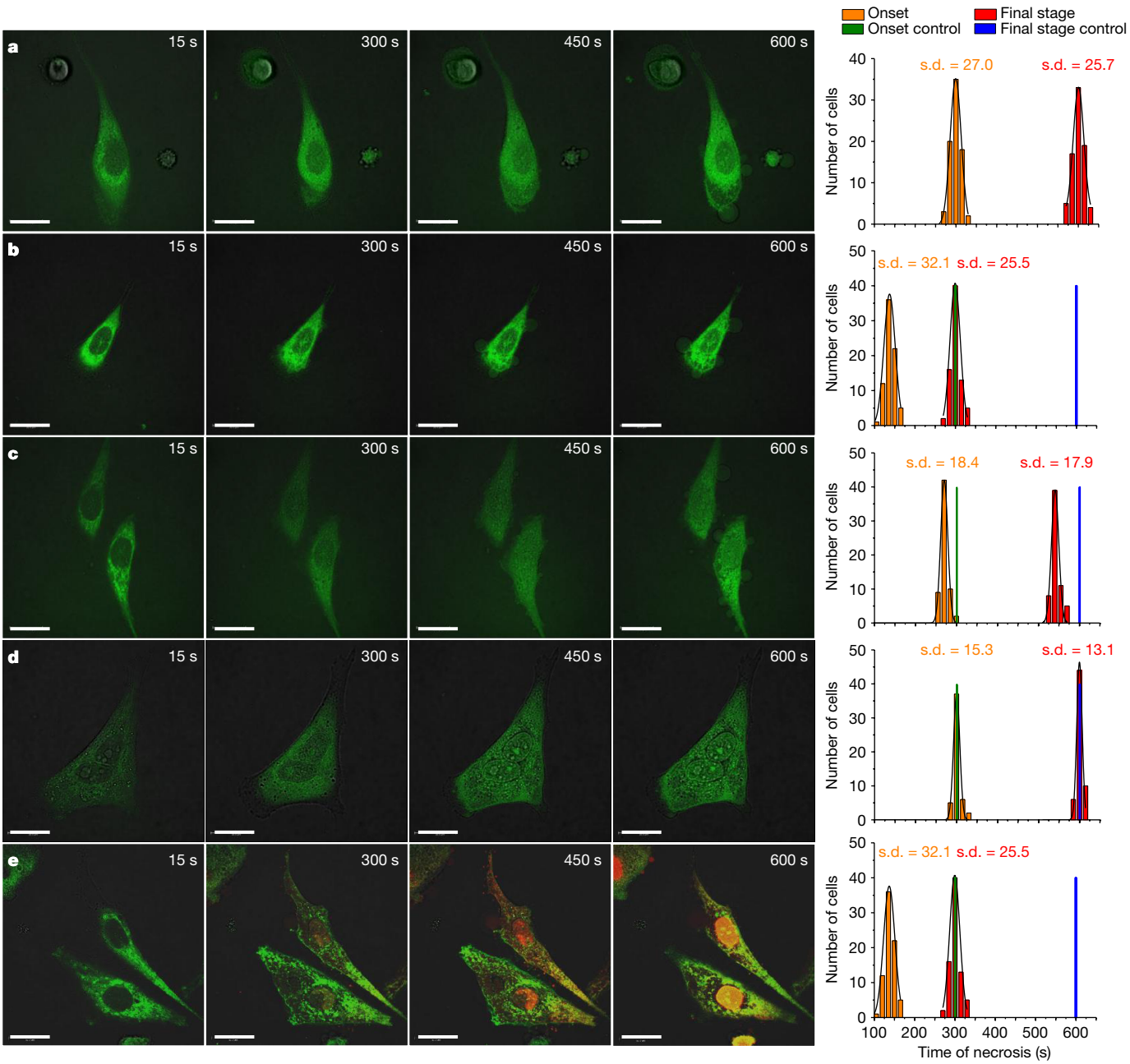

Figure 3 | The effects of nanomachines 3 and 4 and control molecule 5 on PC-3 cells upon UV activation. We recorded the rate of necrotic cell death and permeabilization of analytes into the cells as a function of time (rightmost column). The UV-exposure times are shown in each image (left four columns). **a**–**d**, Blank cells without molecular motors (**a**), with introduction of **3** (**b**) or **4** (**c**), or with non-active **5** (**d**), all at 500 nM with 5 min of incubation before imaging. **e**, Imaging sequence using **3** with the introduction of 100 nM propidium iodide (red, $\lambda_{ex} = 543$ nm, $\lambda_{em} = 610$–630 nm, 0.2 mW), confirming molecular mechanical cell permeabilization with intercalation of RNA and DNA primarily in the cell nuclei. All scale bars, 20 μm. The statistical analyses for each experiment are shown in the rightmost panel. The black curves are Gaussian fits of the raw data, used to determine the mean and standard deviation.

iodide (PI; total concentration of 0.10 μM) was introduced into the cell medium immediately before the time-dependent standardized imaging sequence. PI is a fluorescent intercalating agent that is not internalized by healthy cells and is shown to be non-toxic by our molecular-machine-free controls. Upon membrane disruption by nanomechanical action of **3** (Fig. 3e), PI enters the cell and travels to RNA- and DNA-rich areas, where it intercalates. Its excitation maximum subsequently displays a bathochromic shift of approximately 30 nm (from 535 nm to 565 nm) accompanied by a parallel shift in the hypsochromic emission maximum (from 617 nm to 600 nm), consistent with previously noted trends[21]. Internalized RNA- and DNA-induced PI fluorescence is detected between 600 nm and 630 nm, confirming time-dependent light-activated molecular-motor-induced cell permeabilization. Further, PI was used to follow membrane damage due to UV-activated nanomachine activity as it led to necrosis. Because the entry of the PI occurs on a relatively short timescale compared to that of cell division, the cell has insufficient time to program apoptosis. This lack of apoptosis was confirmed using the apoptosis-specific stain Annexin V: we observed no relevant fluorescence from this dye throughout the course of the experiments.

Considering the observed UV-induced nanomechanical action, we investigated whether the peptide-bearing structures (**7**–**10**) could be used to target specific cells for nanomachine-activated necrosis. The targeted cell line was PC-3, with NIH 3T3 and Chinese hamster ovary

(CHO) cells used as non-targeted controls. We observed no selectivity with the shorter peptide targeting moieties **7** and **8** (Supplementary Table 2, Supplementary Figs 7 and 8). However, using the longer peptide sequences provided by **9** and **10**, the targeted PC-3 cells started to die as a result of UV-activated motor-induced necrosis after 150–180 s, which corresponds to 40%–50% faster onset than for the molecular-motor-free UV-exposed cells or the untargeted molecular motor and cell combinations with NIH 3T3 and CHO cells (Supplementary Table 2, Supplementary Figs 9–12).

Several notable features became apparent in nanomachine design. Physisorption to or insertion into the cell membrane is essential; just being present in the medium will not result in accelerated rotor-induced UV-activated necrosis. With **3**, all three cell types showed accelerated activated necrosis, presumably because the core of **3**, with its smaller addends, interacted well with the membranes and had minimal steric interference while transporting the nanomachines through the membranes. The mono-addended core of **10** is better able to approach the membrane to sufficiently close proximity than is the more sterically hindered **9**, but still not as efficiently as the smaller **3**. Finally, better transport through the membrane was realized with the less sterically encumbered **10** over **9**; doubling the large addends could sterically slow the membrane transport.

We then studied the dynamic effects of nanomechanical action on cellular membranes through the whole-cell patch-clamp electrophysiology of human embryonic kidney 293 cells (HEK293), which are commonly used for electrophysiological interrogation. Using method B, the studies reveal that upon UV activation (355 nm) of molecular motor **3** inward ionic currents were produced that are consistent with hydrophilic pores forming in the cellular membranes. These inward currents were not observed in the absence of UV illumination or during UV illumination of non-rotor-bearing control **5** or of untreated cells (Fig. 4a). Inward currents produced during UV illumination of cells treated with **3** then continued even in the absence of UV illumination, suggesting that the cell membranes were irreversibly damaged. This damage was accompanied by induced morphological changes to the cells, such as membrane blebbing (Fig. 4b, white arrows), cell swelling and cytoplasmic degradation, all indicative of cell death[22]. Although membrane blebbing occurs during apoptosis and necrosis, the large diameter of the blebs observed here (Fig. 4b; radius $r = 3.8 \pm 0.2\,\mu m$, average ± standard deviation) is consistent with necrosis, as is the observed cell swelling and the absence of apoptotic bodies[22,23]. Consistent with the delayed morphological effects that we observed on the other cell lines studied, inward currents in HEK293 cells appeared between 40 s and 60 s after exposure to UV illumination. The slow increase in inward current during illumination suggests an accumulation of many small pores or increasing pore sizes.

Membrane rupture and pore formation under a tangential mechanical force have been studied theoretically and experimentally (see discussion in Supplementary Information). Specific to the nanomechanical forces in our experiments, actuation of the rotor would produce a tangential mechanical force that perturbs the membrane structure[24,25]. The UV photon energy (at wavelength $\lambda = 365$ nm) that actuates the motor is $E = hc/\lambda = 5.4 \times 10^{-19}$ J, where h is Planck's constant and c is the speed of light. If all of this energy is used for force generation, and the linear moving distance of the tip of the rotor is of the order of $s = 1$ nm, then the generated force would be $F = E/s = 0.54$ nN. The stress applied on the membrane would be 540 mN m^{-1}, which greatly exceeds the requisite rupture stress for most bilipid membranes of 1–30 mN m^{-1} (refs 26–28). Even if the nanomechanical action is pulsed and the membrane is more resistant to rupture, it is still theoretically sufficient to disrupt the membrane locally to eventually compromise its integrity. This conclusion is also consistent with the energetics estimation. The estimated free energy for pore formation using molecular dynamics simulations is tens of kilojoules per mole[26,27]. The corresponding UV photon energy is sufficient to disrupt about ten lipid molecules to form a transient pore. Further, the disruption effect of motor actuations might be cumulative. Considering that the rotors (which have sizes of about 1 nm) are small relative to the thickness of the bilipid membranes (7.5–10 nm), the rupture kinetics of the observed nanomechanical opening is not expected to be immediate. This is consistent with our experiments here as well as with the delayed membrane openings

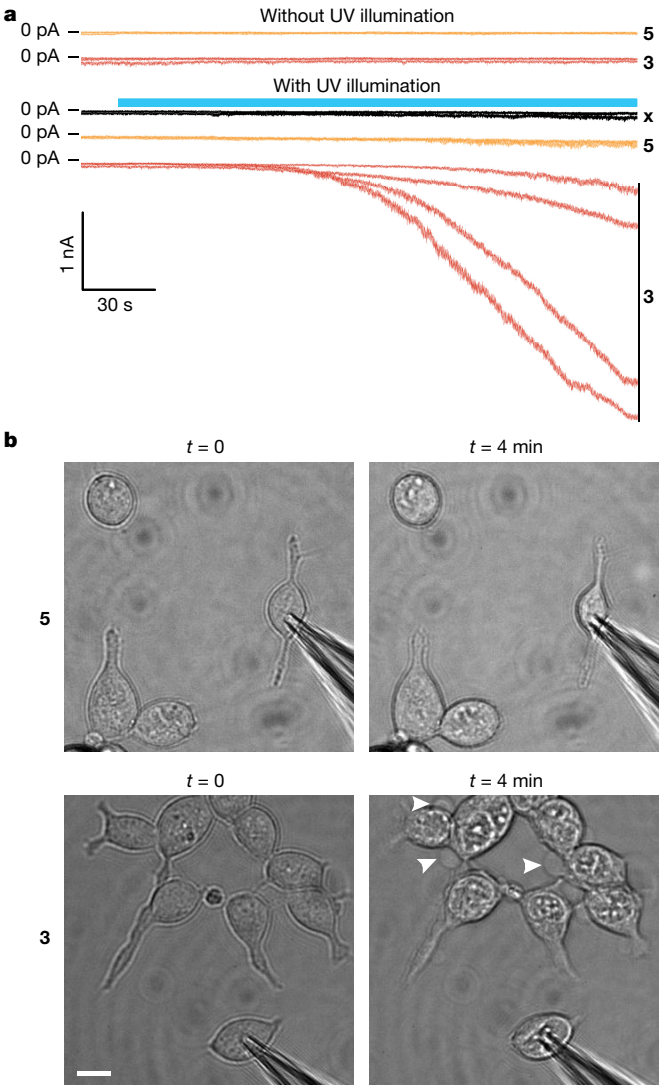

Figure 4 | Whole-cell patch-clamp studies of the dynamic effects of UV-induced molecular mechanical action of 3 on HEK293 cells. Control studies using **3** without UV activation, using UV-exposed rotor-free control molecule **5**, and using no molecular additives (**x**) are also shown. Compounds **3** and **5** were used at 1.0 μM concentrations. **a**, Transmembrane currents in HEK293 cells show that cells treated with UV-activated (355 nm) molecular motor **3** have inward currents that are consistent with membrane degradation (bottom trace). Without UV illumination, cells treated with **3** or **5** show no change in membrane currents over the 4-min recording period (top two traces). Similarly, when using the rotor-free **5** or no molecular additives (**x**), no inward currents are observed during UV illumination (centre two traces). Cells were held at −70 mV in voltage-clamp mode and UV exposure began 15 s after the start of the recording (represented by the blue bar). Each recording is a biological replicate and all traces are shown ($n = 4$ recordings from different cells for **3** with UV illumination; $n = 3$ recordings from different cells for each other condition). **b**, Representative differential interference chromatography images of cells captured before ($t = 0$) and after ($t = 4$ min) exposure to UV illumination in the presence of **3** (bottom) or **5** (top). The white arrows (lower right image) highlight membrane blebbing. Blebbing was observed only in cells treated with UV-activated **3** ($n = 4$ biological replicates) and not in cells treated with **5** and exposed to UV ($n = 3$ biological replicates). The scale bar represents 10 μm and is applicable for each micrograph.

seen previously by others using their probe-induced mechanical perturbations[27–29], noting, however, that probe-tip perturbations are a vertical force model and hence considerably different from the tangential nanomechanical effects applied here[30]. Therefore, nanomechanical action can generate concerted motion on a 1-nm-long molecular rotor that will severely dislocate the membrane molecules, whereas other light-absorbing molecules will merely dissipate the absorbed energy in random motion of atoms in the molecule, underscoring the efficacy of the nanomechanical effect for membrane disruption.

Data Availability All data generated or analysed during this study are included in the paper and its Supplementary Information; Source Data for Figs 2 and 3 are available with the online version of the paper.

Received 7 September 2016; accepted 5 July 2017.

1. Lakshmanan, S. *et al.* Physical energy for drug delivery; poration, concentration and activation. *Adv. Drug Deliv. Rev.* **71,** 98–114 (2014).
2. Chang, D. C. Cell poration and cell fusion using an oscillating electric field. *Biophys. J.* **56,** 641–652 (1989).
3. Liu, D., Wang, L., Wang, Z. & Cuschieri, A. Magnetoporation and magnetolysis of cancer cells via carbon nanotubes induced by rotating magnetic fields. *Nano Lett.* **12,** 5117–5121 (2012).
4. Ivanov, I. T. Spectrofluorometric and microcalorimetric study of the thermal poration relevant to the mechanism of thermohaemolysis. *Int. J. Hyperthermia* **15,** 29–43 (1999).
5. Tachibana, K., Uchida, T., Ogawa, K., Yamashita, N. & Tamura, K. Introduction of cell-membrane porosity by ultrasound. *Lancet* **353,** 1409 (1999).
6. Waleed, M. *et al.* Single-cell optoporation and transfection using femtosecond laser and optical tweezers. *Biomed. Opt. Express* **4,** 1533–1547 (2013).
7. Barber, D. M. *et al.* Optical control of neuronal activity using a light-operated GIRK channel opener (LOGO). *Chem. Sci.* **7,** 2347–2352 (2016).
8. Broichhagen, J. *et al.* Optical control of insulin secretion using an Incretin switch. *Angew. Chem. Int. Ed.* **54,** 15565–15569 (2015).
9. Watson, M. A. & Cockroft, S. L. Man-made molecular machines: membrane bound. *Chem. Soc. Rev.* **45,** 6118–6129 (2016).
10. Xu, T., Gao, W., Xu, L.-P., Zhang, X. & Wang, S. Fuel-free synthetic micro-/nanomachines. *Adv. Mater.* **29,** 1603250 (2017).
11. Haywood-Reid, P. L., Zipf, D. R. & Springer, W. R. Quantification of integrin subunits on human prostatic cell lines—comparison of nontumorigenic and tumorigenic lines. *Prostate* **31,** 1–8 (1997).
12. Collins, A. T., Berry, P. A., Hyde, C., Stower, M. J. & Maitland, N. J. Prospective identification of tumorigenic prostate cancer stem cells. *Cancer Res.* **65,** 10946–10951 (2005).
13. Huang, C. W., Li, Z. & Conti, P. S. *In vivo* near-infrared fluorescence imaging of integrin $\alpha_2\beta_1$ in prostate cancer with cell-penetrating-peptide–conjugated DGEA Probe. *J. Nucl. Med.* **52,** 1979–1986 (2011).
14. Mandelin, J. *et al.* Selection and identification of ligand peptides targeting a model of castrate-resistant osteogenic prostate cancer and their receptors. *Proc. Natl Acad. Sci. USA* **112,** 3776–3781 (2015).
15. García-López, V. *et al.* Unimolecular submersible nanomachines. Synthesis, actuation and monitoring. *Nano Lett.* **15,** 8229–8239 (2015).
16. Pal, R. Phase modulation nanoscopy: a simple approach to enhanced optical resolution. *Faraday Discuss.* **177,** 507–515 (2015).
17. Butler, S. J. *et al.* EuroTracker dyes: design, synthesis, structure and photophysical properties of very bright europium complexes and their use in bioassays and cellular optical imaging. *Dalton Trans.* **44,** 4791–4803 (2015).
18. Kessner, S., Krause, A., Rothe, U. & Bendas, G. Investigation of the cellular uptake of E-Selectin-targeted immunoliposomes by activated human endothelial cells. *Biochim. Biophys. Acta* **1514,** 177–190 (2001).
19. Dunn, W. A., Hubbard, A. L. & Aronson, N. N. Jr. Low temperature selectively inhibits fusion between pinocytic vesicles and lysosomes during heterophagy of ^{125}I-asialofetuin by the perfused rat liver. *J. Biol. Chem.* **255,** 5971–5978 (1980).
20. Purcell, E. M. Life at low Reynolds number. *Am. J. Phys.* **45,** 3–11 (1977).
21. Lecoeur, H. Nuclear apoptosis detection by flow cytometry: influence of endegenous endonucleases. *Exp. Cell Res.* **277,** 1–14 (2002).
22. Elmore, S. Apoptosis: a review of programmed cell death. *Toxicol. Pathol.* **35,** 495–516 (2007).
23. Barros, L. F. *et al.* Apoptotic and necrotic blebs in epithelial cells display similar neck diameters but different kinase dependency. *Cell Death Differ.* **10,** 687–697 (2003).
24. Chen, J., Kistemaker, J. C. M., Robertus, J. & Feringa, B. L. Molecular stirrers in action. *J. Am. Chem. Soc.* **136,** 14924–14932 (2014).
25. Sandre, O., Moreaux, L. & Brochard-Wyart, F. Dynamics of transient pores in stretched vesicles. *Proc. Natl Acad. Sci. USA* **96,** 10591–10596 (1999).
26. Li, F., Chan, C. U. & Ohl, C. D. Yield strength of human erythrocyte membranes to impulsive stretching. *Biophys. J.* **105,** 872–879 (2013).
27. Evans, E. & Smith, B. A. Kinetics of hole nucleation in biomembrane rupture. *New J. Phys.* **13,** 095010 (2011).
28. Shigematsu, T., Koshiyama, K. & Wada, S. Effects of stretching speed on mechanical rupture of phospholipid/cholesterol bilayers: molecular dynamics simulation. *Sci. Rep.* **5,** 15369 (2015).
29. Bennett, W. F. D., Sapay, N. & Tieleman, D. P. Atomistic simulations of pore formation and closure in lipid bilayers. *Biophys. J.* **106,** 210–219 (2014).
30. Wang, X., Shindel, M. S., Wang, S.-W. & Ragan, R. Elucidating driving forces for liposome rupture: external perturbations and chemical affinity. *Langmuir* **28,** 7417–7427 (2012).

Supplementary Information is available in the online version of the paper.

Acknowledgements G.W. acknowledges North Carolina State University start-up funds and the FRPD Award. R.P. acknowledges support from the Royal Society and BSI Durham. J.M.T. acknowledges support from the National Science Foundation (CHE-1007483). Imaging for this project was supported by the Integrated Microscopy Core at Baylor College of Medicine with funding from NIH (DK56338 and CA125123), CPRIT (RP150578), the Dan L. Duncan Comprehensive Cancer Center and the John S. Dunn Gulf Coast Consortium for Chemical Genomics. We thank R. S. Gunasekera for his assistance with imaging and A. Marti for the use of his high-performance liquid chromatography (HPLC) system for the separation of **7**–**10**. W. Sikkema prepared Fig. 1a.

Author Contributions The idea to use the nanomachines to open membranes was suggested by J.M.T., then further discussed with G.W. and R.P. V.G.-L. carried out the synthesis of **1**–**13** and **16** and L.G.N. carried out the synthesis of **14**, both under the supervision of J.M.T. F.C. performed the experiments on lipid vesicles under the supervision of G.W. R.P. carried out all of the experiments on live cells. A.A. and V.G.-L. carried out the HPLC separation of **7**–**10**. A.B.K. and G.W. developed the theory. G.D. performed the patch-clamp work under the supervision of J.T.R.; G.D. and J.T.R. also prepared the text for that section. V.G.-L., G.W., R.P. and J.M.T. wrote the manuscript. All authors read and approved the manuscript.

Author Information Reprints and permissions information is available at www.nature.com/reprints. The authors declare no competing financial interests. Readers are welcome to comment on the online version of the paper. Publisher's note: Springer Nature remains neutral with regard to jurisdictional claims in published maps and institutional affiliations. Correspondence and requests for materials should be addressed to J.T.R. (jtrobinson@rice.edu), G.W. (gufeng_wang@ncsu.edu), R.P. (robert.pal@dur.ac.uk) or J.M.T. (tour@rice.edu).

Reviewer Information *Nature* thanks R. D. Astumian, S. Cockroft and the other anonymous reviewer(s) for their contribution to the peer review of this work.

nature research

Corresponding Author: Guillaume Duret, Jacob Robinson and Robert P

Date: 16/06/2017

Life Sciences Reporting Summary

Nature Research wishes to improve the reproducibility of the work we publish. This form is published with all life science papers and is intended to promote consistency and transparency in reporting. All life sciences submissions use this form; while some list items might not apply to an individual manuscript, all fields must be completed for clarity.

For further information on the points included in this form, see Reporting Life Sciences Research. For further information on Nature Research policies, including our data availability policy, see Authors & Referees and the Editorial Policy Checklist.

Experimental design

1. Sample size

   Describe how sample size was determined.

   Sample size have been determined in order to provide a statistically significant sample cohort with numbers to ensure reproducibility

2. Data exclusions

   Describe any data exclusions.

   No data was excluded

3. Replication

   Describe whether the experimental findings were reliably reproduced.

   Yes: Sample size have been determined in order to provide a statistically significant sample cohort with numbers and 3-5 individual repeats to ensure reproducibility with each cell line and experimental condition. Electrophysiology recordings were performed on different days on independent cell cultures.

4. Randomization

   Describe how samples/organisms/participants were allocated into experimental groups.

   N/A

5. Blinding

   Describe whether the investigators were blinded to group allocation during data collection and/or analysis.

   N/A

Note: all studies involving animals and/or human research participants must disclose whether blinding and randomization were used.

6. Statistical parameters

   For all figures and tables that use statistical methods, confirm that the following items are present in relevant figure legends (or the Methods section if additional space is needed).

n/a	Confirmed	
☐	☒	The exact sample size (*n*) for each experimental group/condition, given as a discrete number and unit of measurement (animals, litters, cultures, etc.)
☐	☒	A description of how samples were collected, noting whether measurements were taken from distinct samples or whether the same sample was measured repeatedly.
☐	☒	A statement indicating how many times each experiment was replicated
☐	☒	The statistical test(s) used and whether they are one- or two-sided (note: only common tests should be described solely by name; more complex techniques should be described in the Methods section)
☒	☐	A description of any assumptions or corrections, such as an adjustment for multiple comparisons
☒	☐	The test results (e.g. *p* values) given as exact values whenever possible and with confidence intervals noted
☐	☒	A summary of the descriptive statistics, including central tendency (e.g. median, mean) and variation (e.g. standard deviation, interquartile range)
☒	☐	Clearly defined error bars

See the web collection on statistics for biologists for further resources and guidance.

Software

Policy information about availability of computer code

7. Software

Describe the software used to analyze the data in this study.	Origin2015 Pro, ImageJ and Clampfit (Molecular Device)

For all studies, we encourage code deposition in a community repository (e.g. GitHub). Authors must make computer code available to editors and reviewers upon request. The *Nature Methods* guidance for providing algorithms and software for publication may be useful for any submission.

Materials and reagents

Policy information about availability of materials

8. Materials availability

Indicate whether there are restrictions on availability of unique materials or if these materials are only available for distribution by a for-profit company.	N/A

9. Antibodies

Describe the antibodies used and how they were validated for use in the system under study (i.e. assay and species).	N/A

10. Eukaryotic cell lines

a. State the source of each eukaryotic cell line used.	Cell lines were sourced from ATCC (NIH 3T3 CRL-1658, PC3 CRL-1435, CHO(-K1) CCL-61 and HEK293 cells CRL-1573 from ATCC)
b. Describe the method of cell line authentication used.	ATCC's STR protocol and report
c. Report whether the cell lines were tested for mycoplasma contamination.	Periodic test have been conducted on all cell lines as a routine laboratory protocol before each individual experiment.
d. If any of the cell lines used in the paper are listed in the database of commonly misidentified cell lines maintained by ICLAC, provide a scientific rationale for their use.	PC3 cell lines are identified as diluting cell lines for 3 other prostate cell lines BUT PC3 cell line itself in not listed as such.

Animals and human research participants

Policy information about studies involving animals; when reporting animal research, follow the ARRIVE guidelines

11. Description of research animals

Provide details on animals and/or animal-derived materials used in the study.	N/A

Policy information about studies involving human research participants

12. Description of human research participants

Describe the covariate-relevant population characteristics of the human research participants.	N/A